HOSTEL ID: 84

Martian Core Analysis

Kriti'25

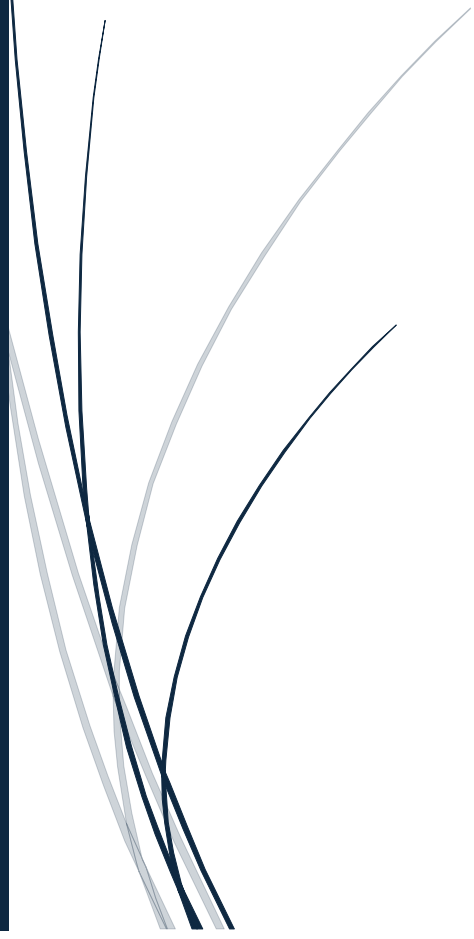

Table of Contents

Module 1: Understanding Seismic Wave Velocities

P-waves (Primary waves)

- **Nature**: P-waves are longitudinal or compressional waves. The particle motion is parallel to the direction of wave propagation.

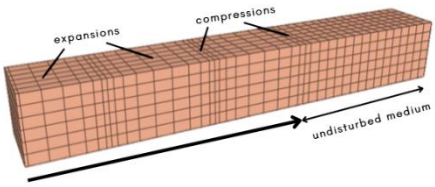

- **Speed**: P-waves are the fastest seismic waves.
- **Propagation Medium**: They can travel through solids, liquids and gases.
- **Material Interaction**: As they propagate, P-waves compress and expand the material they travel through, causing changes in the material's volume.

S-waves (Secondary waves)

- **Nature**: S-waves are transverse or shear waves. The particle motion is perpendicular to the direction of wave propagation.

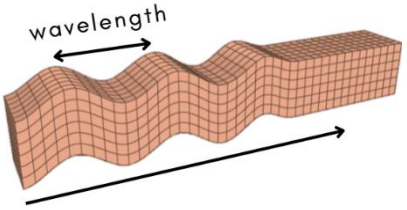

- **Speed**: S-waves are slower than P-waves but are faster than surface waves.
- **Propagation Medium**: They can only travel through solids because liquids and gases do not support shear stress.
- **Material Interaction**: S-waves cause shear deformation of the material they propagate through, but they do not change its volume.

Key Differences

- **Speed**: P-waves are faster than S-waves.
- **Motion**: P-waves involve compressions and rarefactions (longitudinal), while S-waves involve shearing (transverse).
- **Medium**: P-waves can propagate through all states of matter, while S-waves require a solid medium.

These properties make P-waves and S-waves important for understanding the Earth's interior structure, as their behaviour reveals information about the materials they meet.

Wave Equation Derivation

Given Wave Equation:

$$\rho \frac{\partial^2 u_i}{\partial t^2} = \frac{\partial \sigma_{ij}}{\partial x_j} \dots\dots\dots (1)$$

Hooke's Law:

$$\sigma_{ij} = \lambda \delta_{ij} (\nabla \cdot \vec{u}) + \mu \left(\frac{\partial u_i}{\partial x_j} + \frac{\partial u_j}{\partial x_i} \right) \dots\dots\dots (2)$$

Substituting (2) into (1):

$$\rho \frac{\partial^2 u_i}{\partial t^2} = \lambda \frac{\partial}{\partial x_j} \left[\delta_{ij} (\nabla \cdot \vec{u}) \right] + \mu \frac{\partial}{\partial x_j} \left(\frac{\partial u_i}{\partial x_j} + \frac{\partial u_j}{\partial x_i} \right) \dots\dots\dots (3)$$

Expanding $\nabla \cdot \vec{u}$:

$$\nabla \cdot \vec{u} = \frac{\partial u_1}{\partial x_1} + \frac{\partial u_2}{\partial x_2} + \frac{\partial u_3}{\partial x_3} = \frac{\partial u_i}{\partial x_i} \dots\dots\dots (4)$$

Rewriting the Equation:

$$\rho \frac{\partial^2 u_i}{\partial t^2} = \lambda \frac{\partial}{\partial x_i} \left(\delta_{ij} \frac{\partial u_j}{\partial x_j} \right) + \mu \nabla^2 u_i + \mu \frac{\partial}{\partial x_i} (\nabla \cdot \vec{u}) \dots\dots\dots (5)$$

Expanding Kronecker Delta Terms:

$$\frac{\partial}{\partial x_i}\left(\delta_{ij}\frac{\partial u_j}{\partial x_j}\right) = \delta_{11}\frac{\partial^2 u_1}{\partial x_1^2} + \delta_{12}\frac{\partial^2 u_1}{\partial x_2^2} + \delta_{13}\frac{\partial^2 u_1}{\partial x_3^2}$$
$$+\delta_{21}\frac{\partial^2 u_2}{\partial x_1^2} + \delta_{22}\frac{\partial^2 u_2}{\partial x_2^2} + \delta_{23}\frac{\partial^2 u_2}{\partial x_3^2}$$
$$+\delta_{31}\frac{\partial^2 u_3}{\partial x_1^2} + \delta_{32}\frac{\partial^2 u_3}{\partial x_2^2} + \delta_{33}\frac{\partial^2 u_3}{\partial x_3^2} \dots\dots\dots (6)$$

Property of Kronecker Delta:

$$\delta_{ij} = \begin{cases} 1, & \text{if } i = j \\ 0, & \text{otherwise} \end{cases}$$

Simplification:

$$\delta_{ij}\frac{\partial u_j}{\partial x_j} = \frac{\partial u_i}{\partial x_i} = \nabla \cdot \vec{u} \dots\dots\dots (7)$$

Final Form:

$$\rho\frac{\partial^2 u_i}{\partial t^2} = (\lambda + \mu)\frac{\partial}{\partial x_i}(\nabla \cdot \vec{u}) + \mu\nabla^2 u_i \dots\dots\dots (8)$$

P-Waves and S-Waves

For P-Waves:

- $\nabla \cdot \vec{u} \neq 0$
- $\nabla \times \vec{u} = 0$

The equation becomes:

$$\rho\frac{\partial^2 u_i}{\partial t^2} = (\lambda + 2\mu)\frac{\partial^2 u_i}{\partial x_i^2} \dots\dots\dots (9)$$

Velocity of P-waves is:

$$v_p = \sqrt{\frac{\lambda + 2\mu}{\rho}} \dots\dots\dots (10)$$

For S-Waves:

- $\nabla \cdot \vec{u} = 0$
- $\nabla \times \vec{u} \neq 0$

The equation becomes:

$$\rho \frac{\partial^2 u_i}{\partial t^2} = \mu \nabla^2 u_i \dots\dots\dots (11)$$

Velocity of S-waves is:

$$v_s = \sqrt{\frac{\mu}{\rho}} \dots\dots\dots (12)$$

Bulk Modulus: $K = \lambda + \frac{2}{3}\mu$

Shear Modulus: $G = \mu$

Therefore, velocities in terms of Bulk and Shear Modulus:

$$v_p = \sqrt{\frac{K + \frac{4}{3}G}{\rho}} \dots\dots\dots (13)$$

$$v_s = \sqrt{\frac{G}{\rho}} \dots\dots\dots (14)$$

Module 2: Identifying Shadow Zones on Mars

1. What is the "S-wave shadow zone" and why does its existence indicate the presence of a liquid core in Mars?

The S-wave shadow zone on Mars is a region where seismic S-waves are not detected. It offers critical insights into the internal structure of the planet, specifically the nature of its core.

- **S-wave Properties**: S-waves, or shear waves, propagate as transverse waves and require a solid medium to travel. Liquids cannot sustain shear stresses, so S-waves cannot pass through liquid regions.
- **Core Interaction**: If Mars has a liquid core, S-waves would be absorbed at the core-mantle boundary, creating a shadow zone where these waves are absent.
- **Shadow Zone Range**: The detection of an S-wave shadow zone would depend on the size and properties of Mars' core. Seismometers on Mars, such as those deployed by NASA's InSight mission are key to finding these patterns.
- **Implications for Core Composition**: The presence of an S-wave shadow zone on Mars strongly indicates that the planet has a partially or fully liquid core. This finding provides evidence about the thermal state and composition of Mars' interior, including the presence of lighter elements such as sulphur in the core.

2. If S-waves are not detected on the opposite side of Mars from a seismic event, what can you infer about the core's state?

If S-waves from a seismic event are absent on the opposite side of Mars, the following inferences can be made:

- **Liquid Core**: The absence of S-waves strongly supports the hypothesis that Mars has a liquid core, as S-waves are absorbed rather than transmitted through liquid regions.
- **Core Size and Structure**: The extent of the S-wave shadow zone can provide constraints on the size and geometry of the liquid core. A larger shadow zone implies a larger core.
- **Seismic Velocity Contrast**: The sharp contrast in seismic wave velocities at the core-mantle boundary also helps to estimate the core's composition and density.

These observations contribute to a better understanding of Mars' geophysical processes and its evolution as a terrestrial planet.

Module 3: Calculating the Core-Mantle Boundary (CMB)

1. Snell's Law to Explain P-Wave Refraction at the Core-Mantle Boundary

Snell's Law defines how the direction of a seismic wave changes as it crosses the boundary between two distinct rock layers with varying seismic velocities. It is expressed as:

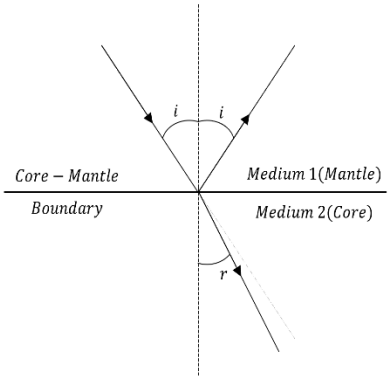

$$\frac{\sin i}{\sin r} = \frac{v_1}{v_2}$$

where:

- i: angle of incidence,
- r: angle of refraction,
- v_1: velocity of P-wave in the first medium (mantle),
- v_2: velocity of P-wave in the second medium (core).

As P-waves propagate from the mantle into the core, they encounter the core-mantle boundary, where a reduction in seismic wave velocity occurs (e.g., from $v_1 = 10$ km/s in the mantle to $v_2 = 8$ km/s in the core). Due to this reduction in velocity, the waves undergo refraction away from the boundary.

2. Calculating the Angle of Refraction

Given: $v_1 = 10\ km/s, \quad v_2 = 8\ km/s, \quad i = 30°$

Snell's Law is applied as follows:

$$\frac{\sin i}{\sin r} = \frac{v_1}{v_2}$$

By substituting the given values:

$$\frac{\sin 30^\circ}{\sin r} = \frac{10}{8}$$

Simplifying:

$$\sin r = \frac{\sin 30^\circ \cdot 8}{10}$$

$$\sin r = \frac{0.5 \cdot 8}{10} = 0.4$$

Solving for r:

$$r = \sin^{-1} 0.4 \approx 23.58^\circ$$

Thus, the angle of refraction is determined to be $r = 23.58^\circ$

Module 4: Determining Core Radius

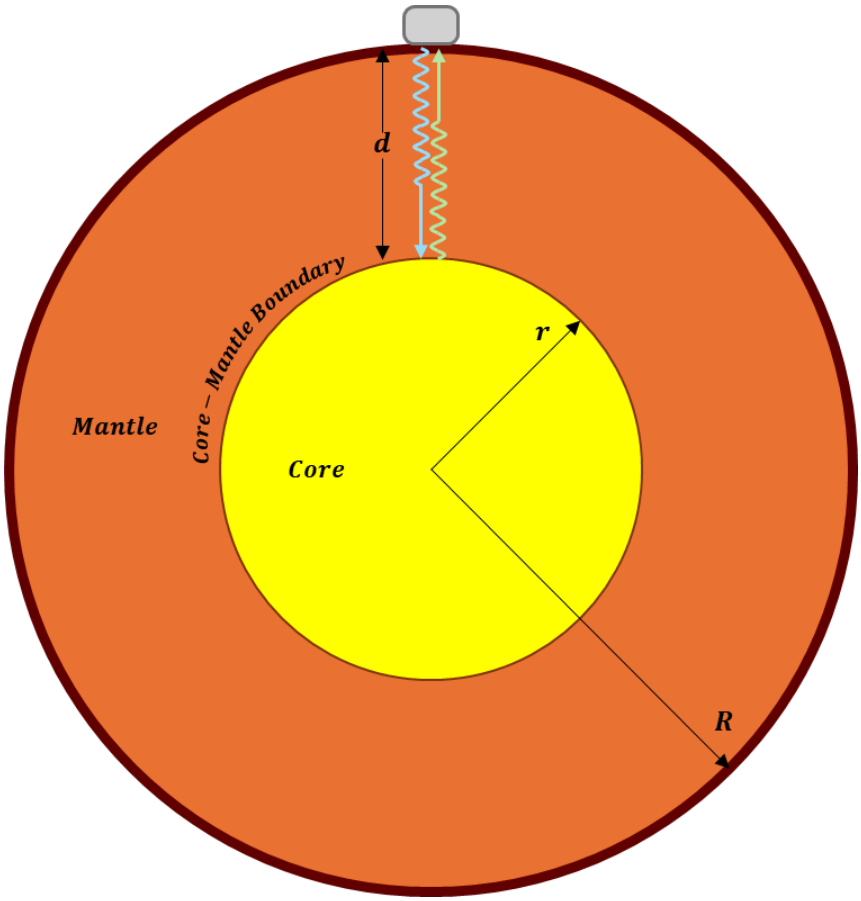

The total radius of Mars is provided as $R = 3390$ km, and the depth to the core-mantle boundary is $d = 560$ km. By applying the formula for the core radius:

$$R_c = R - d$$

the calculation is performed as follows:

$$R_c = 3390\,km - 560\,km = 2830\,km$$

Verification:

The verification process is conducted using data obtained from the InSight mission. The detected vibrations, which

originate at the surface, travel to the core, and reflect back, cover a total distance of twice the depth to the core-mantle boundary $(2 \cdot d)$. The P-wave is recorded first, followed by the S-wave.

Time taken by P-wave is: $t_p = \frac{2 \cdot d}{v_p}$, v_p: P-wave velocity.

Time taken by S-wave is: $t_s = \frac{2 \cdot d}{v_s}$, v_s: P-wave velocity.

The difference between arrival times of S-wave and P-wave, $t_s - t_p$, provides an estimate for d. The value of $t_s - t_p$ is obtained from the NASA InSight Mission data, which records it as approximately 400–450 seconds:

$$t_s - t_p = 2 \cdot d \cdot \left(\frac{1}{v_s} - \frac{1}{v_s}\right)$$

By assuming the theoretical values $v_s = 1825\, m/s$, $v_p = 3579\, m/s$, the depth d is found to be approximately $744.77\, km$. This result aligns closely with theoretical predictions, although a slight deviation from the original value is observed.

Module 5: Verifying Core State

Based on your calculations and observations from previous modules, summarize whether the Martian core is solid or liquid. Justify your answer using the absence of S-waves and the reduction in P-wave velocity within the core.

Absence of S-Waves:

S-waves (shear waves) are a type of seismic wave that can only propagate through solid materials i.e. they are unable to travel through liquids or gases. In seismic studies of Mars, a notable absence of S-waves passing through the core has been observed. This absence indicates that the Martian core does not support the transmission of S-waves, suggesting a liquid state.

Reduction in P-Wave Velocity:

P-waves (primary waves) are compressional seismic waves capable of moving through both solid and liquid materials. However, their velocity is influenced by the medium they traverse. Typically, P-waves travel faster through solids due to the higher rigidity and incompressibility of solid materials. In the case of Mars, seismic data has shown a reduction in P-wave velocity upon entering the core. This decrease in speed is consistent with the transition from a solid mantle to a less rigid, liquid core.

Supporting Evidence:

Further supporting the liquid nature of Mars's core, studies have detected reflections of seismic waves at the core-mantle boundary. This, combined with geodetic data, have been used

to estimate the radius of the liquid metal core, therefore reinforcing the conclusion of its liquid state.

In summary, the absence of S-waves traversing the core and the observed reduction in P-wave velocity upon entering the core provide compelling evidence that Mars' core is in a liquid state.

Module 6: Seismic Signal Processing Using ML

1. Introduction

Seismic data, which records the vibrations caused by natural phenomena like earthquakes or artificial sources, contains valuable information about Earth's subsurface structure. In this module, we focus on leveraging machine learning (ML) techniques to analyse seismic waveforms and infer crucial geological properties, specifically related to the Earth's core, and we determine whether a target point is in the shadow of a given seismic event source using a geometric criterion and then classify these conditions using a Random Forest classifier..

2. Methodology

2.1. Simulating Seismic Waveforms Based on the Wave Equation

To simulate seismic waveforms using the wave equation, we'll:

- Define the physical properties of the medium (e.g., density, Lamé parameters).
- Compute the P-wave velocity (V_p) and S-wave velocity (V_s).
- Generate seismic waveforms for P-waves and S-waves using sinusoidal functions, incorporating amplitude attenuation, phase shifts, and frequency.

2.1.1. Assume a Plane Wave Solution

$$u_i(x,t) = A\, e^{i(kx-\omega t+\phi)}$$

where:

- A: Amplitude of the wave,
- k: Wave number
- ω: Angular frequency
- ϕ: Phase shift

2.1.2. Substitute into the Wave Equation

P-wave:

- P-waves are compressional waves, where the displacement vector u_i is parallel to the direction of propagation ($\nabla \cdot \vec{u} \neq 0, \nabla \times \vec{u} = 0$)
- wave velocity

$$V_p = \sqrt{\frac{\lambda + 2\mu}{\rho}}$$

- The equation becomes:

$$u_p(x,t) = A_p e^{i(k_p x - \omega_p t + \phi_p)}$$

S-wave:

- S-waves are compressional waves, where the displacement vector u_i is parallel to the direction of propagation ($\nabla \cdot \vec{u} = 0, \nabla \times \vec{u} \neq 0$)
- wave velocity

$$V_p = \sqrt{\frac{\mu}{\rho}}$$

- The equation becomes:

$$u_s(x,t) = A_s e^{i(k_s x - \omega_s t + \phi_s)}$$

2.1.3. Frequency

From the wave equation, the frequency f of a wave is not directly "fixed." Instead, it depends on:

- Material properties (Lame's parameters λ, μ and density ρ)
- Wave velocity (v_p, v_s)
- Wavelength (λ)

Therefore, we can obtain frequency f, as:

$$f = v/\lambda$$

where:

- v: velocity
- λ: wavelength

2.1.4. Realistic attenuation

In real materials, seismic waves lose energy as they propagate due to:

- Scattering (interaction with inhomogeneities),
- Viscoelasticity (material damping).

This attenuation is modelled as an exponential decay of amplitude:

$$A(x) = A_0 e^{-\alpha x}$$

where:

- A_0: Initial amplitude,
- α: Attenuation coefficient (material-dependent),
- x: Distance travelled by the wave.

Key factors:

- Material properties: attenuation coefficient α depends on the medium's physical properties, such as its viscosity and density.
- Wave type: S-waves tend to attenuate more than P-waves in most materials.

2.1.5. Phase shift

The phase $\phi(x,t)$ of a wave represents the oscillation cycle at a given point in space and time. When a wave encounters a boundary (e.g., the core-mantle boundary), part of the wave is reflected, and part is transmitted. This causes a phase shift.

$$\Delta\phi_{reflection} = \pi, \qquad \Delta\phi_{refraction} = k_2 x_2 - k_1 x_1$$

where:

- k_1, k_2: Wave numbers before and after the boundary,
- x_1, x_2: Distances travelled in the two layers.

To account for differences in arrival times and interactions with subsurface structures (e.g., core-mantle boundary), a phase shift ϕ is introduced for S-waves.

2.1.6. Combined Formulae

Using the wave equation and considering attenuation and phase effects, the wave can be described as:

$$u(x,t) = A_0 e^{-\alpha x} e^{i(kx - \omega t + \Delta\phi)}$$

2.2. Shadow Detection Function

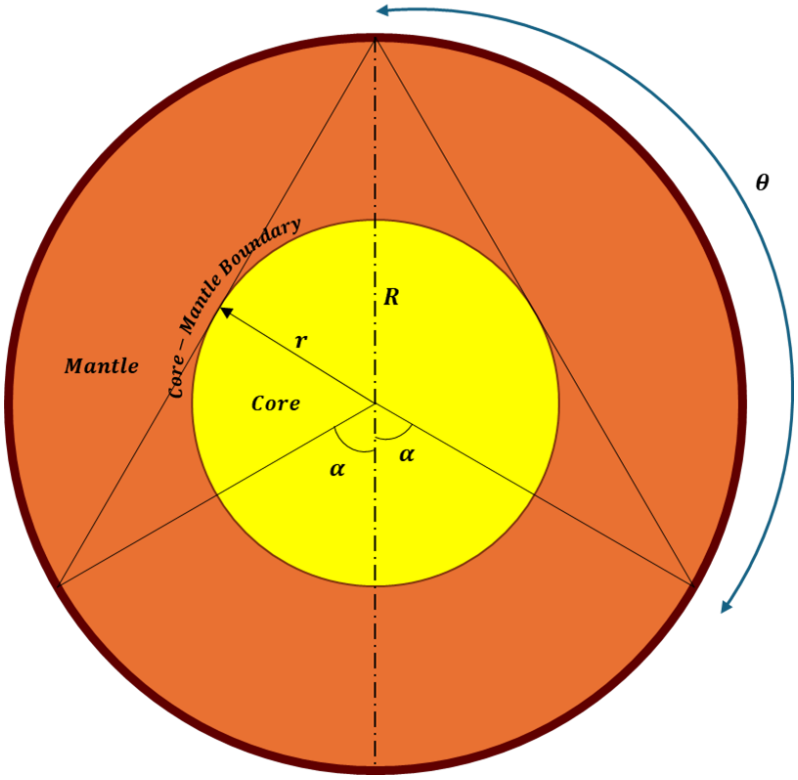

2.2.1. Angular Threshold calculation

$$\sin\frac{\alpha}{2} = \frac{r}{R}$$

Shadow zone iff $\theta > 180° - \alpha$

Threshold angle = $180° - \alpha$

It is known that $\cos\alpha = 1 - 2 \cdot \frac{r^2}{R^2}$

$\Rightarrow$ threshold angle $= \cos^{-1}\left(2 \cdot \frac{r^2}{R^2} - 1\right)$,

$\theta >$ threshold angle

2.2.2. Angular Distance Calculation

The angular distance between the source and the target is calculated using the haversine formula:

$$\theta = \cos^{-1}(\sin(\phi_1) \cdot \sin(\phi_2) + \cos(\phi_2) \cdot \cos(\lambda_2 - \lambda_1))$$

Here ϕ_1 and ϕ_2 represent the latitudes of the source and the target.

λ_1 and λ_2 represent longitude.

2.2.3. Shadow Detection

The angular distance between the source and the target is calculated in the domain of [0, π]. If the angular distance is greater than the threshold angle calculated, then the target lies in the S-wave shadow zone. If not, it is in non-shadow zone.

2.3. Flagging Data

The available data consists of four columns: the latitude and longitude of the source and the latitude and longitude of the epicentre. The shadow detection function is then applied to each data point, flagging it as 1 if a shadow exists and 0 if it does not. Consequently, the target variable is created.

2.4. Model Training

1. We first tried models like logistic regression but because the data doesn't have linear relationship, logistic regression finds it hard to get a decision boundary. Thus we decided to move with the RandomForest approach.
2. The dataset contained into features of source_latitude, source_longitude, target_latitude, target_longitude and labels of 0/1.
3. Data was split 80-20 into train and test datasets.
4. A Random Forest Classifier of 100 estimators was trained to classify shadow zone conditions.

5. Training and test accuracies were computed to evaluate the performance of the model.

3. Results

The model performance was as follows:

- Training Accuracy: 100%
- Test Accuracy: 99.8%

This shows that the model generalizes well to unseen data and can accurately predict shadow conditions.

4. Challenges Faced

4.1. Geometric Complexity

- Accurate spherical trigonometry is required to determine whether the point lies in the shadow zone.
- Careful considerations and calculations, based on Mars' planetary structure, were involved in defining the threshold angle.

4.2. Computational Load

- Intense computation was required for calculating the shadow zone detection function of such a large dataset.
- Performance optimization was achieved using NumPy and Pandas libraries.

4.3. Model Selection

Logistic regression and other linear classifiers were not applied due to the highly nonlinear nature of the decision boundary for shadow classification. Random Forest was chosen because it allows complex decision boundaries

and interactions between variables to be modeled more effectively than linear methods.

5. Conclusion

This project successfully implemented a shadow classification model using planetary geometry and machine learning. The Random Forest classifier provided highly accurate predictions, making it a reliable tool for shadow classification on Mars. Future work could explore deep learning approaches and more refined planetary models for improved generalization and interpretability.

Module 7: Predicting Martian Core Radius Using a Regression

1. Introduction

The primary objective of this module was to predict the core radius of a Martian-like planet using a machine learning approach. To achieve this, synthetic data was generated based on fundamental principles from planetary seismology. The focus was placed on modelling the relationship between seismic wave velocities (S-wave and P-wave), material properties (such as shear modulus, density, and Lame's first parameter), and seismic travel times. These variables were utilized as features for training a Random Forest Regressor, a model that is well-suited for capturing non-linear relationships in complex datasets.

2. Methodology

2.1. Data Generation

2.1.1. Synthetic Parameter Sampling

Realistic ranges for the physical parameters were selected based on theoretical and observational data from planetary seismology:

- Shear modulus (μ): 10 to 50 GPa
- Density (ρ): 2500 to 8000 kg/m³
- Lame's first parameter (λ): 20 to 80 GPa

2.1.2. Seismic Velocities

The seismic velocities, V_p (P-wave) and V_s (S-wave), were calculated using the following equations:

$$V_p = \sqrt{\frac{\lambda + 2\mu}{\rho}}, \qquad V_s = \sqrt{\frac{\mu}{\rho}}$$

These velocities were constrained to realistic ranges:

- V_p: 1500-12000 m/s
- V_s: 500-5000 m/s

2.1.3. Core Depth and Radius

The core depth (d) was sampled from a normal distribution with a mean of 1690 km and a standard deviation of 100 km and clipped to the range of 1390–1990 km to maintain physical validity. The core radius was computed as:

$$Core\ Radius\ =\ 3390\,km\ -\ d$$

2.1.4. Feature Engineering

In planetary seismology, the travel time difference between the S-wave and P-wave, denoted as $t_s - t_p$, is crucial for determining the core radius. The relationship is given by the equation:

$$t_s - t_p = 2d\left(\frac{1}{v_s} - \frac{1}{v_p}\right)$$

where:

- $t_s - t_p$: The difference in travel times for the S-wave and P-wave.
- d: The core depth.
- v_s and v_p: The S-wave and P-wave velocities.

An additional feature $\frac{1}{v_s} - \frac{1}{v_p}$, was also included to enhance predictive power.

2.2. Modelling

2.2.1. Regression Model

A Random Forest Regressor was chosen for its ability to model complex, non-linear relationships between the features and target variable (core radius). The model was trained using an 80%-20% train-test split.

2.2.2. Evaluation Metrics

The performance of the model was assessed using the following metrics:

- Mean Absolute Error (MAE)
- Mean Squared Error (MSE)
- R^2 Score

2.3. Visualization

The results were visualized using the following methods:

- Scatter plots comparing actual and predicted core radii.
- Residual analysis to assess the error distribution.
- Histogram of predicted core radii.

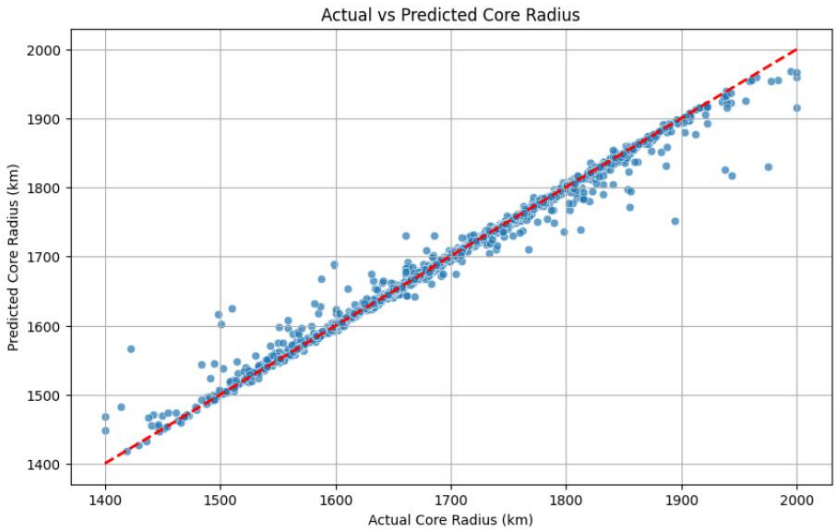
Actual vs Predicted Core Radius
Predicted Core Radius (km)
Actual Core Radius (km)
2000
1900
1800
1700
1600
1500
1400
1400
1500
1600
1700
1800
1900
2000

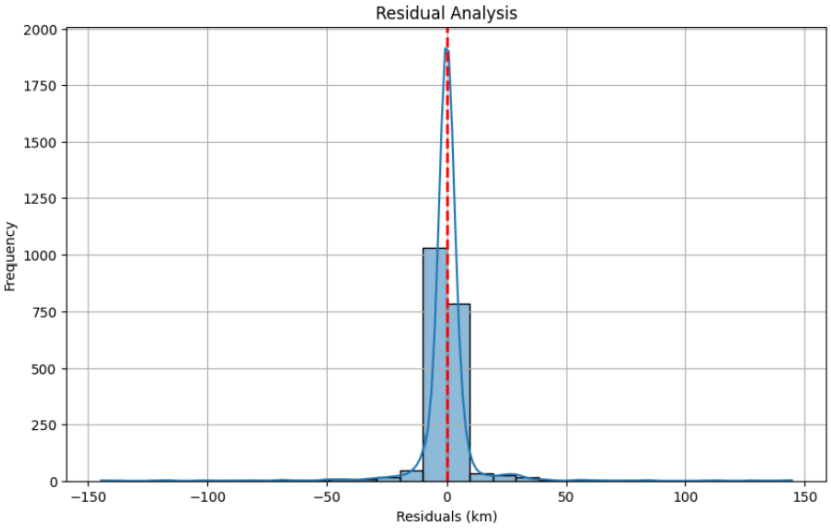
Residual Analysis
Frequency
Residuals (km)
2000
1750
1500
1250
1000
750
500
250
0
−150
−100
−50
0
50
100
150

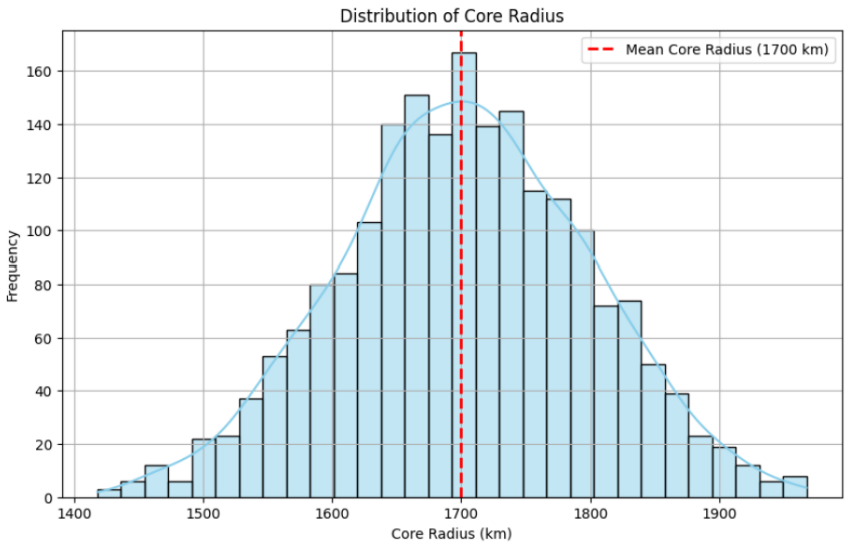
Distribution of Core Radius
Mean Core Radius (1700 km)
Frequency
Core Radius (km)
160
140
120
100
80
60
40
20
0
1400
1500
1600
1700
1800
1900

3. Results

3.1. Model Performance

The model's performance metrics was as follows:

- MAE: 6.54 km
- MSE: 59.87 km^2
- R^2 Score: 0.92

3.2. Representative Predictions

For an input consisting of $t_s - t_p$ = 400 s, feature = 0.00045, and density = 4000 kg/m^3, the predicted core radius was 1996.18 km.

3.3. Visual Insights

- The scatter plot shows a strong linear relationship between actual and predicted core radii, with minimal deviations.
- Residual analysis indicated a symmetric distribution centred around zero, with no significant skewness or outliers, suggesting that the model's errors are random and not biased.
- The predicted core radius values exhibited a plausible distribution, with a peak near the expected mean.

4. Challenges Faced

4.1. Data Generation

One of the primary challenges encountered was ensuring that the synthetic dataset reflected realistic physical scenarios. The calibration of parameter ranges and their

interdependencies required careful consideration to maintain valid core depth and radius values.

4.2. Feature Engineering

Determining and designing meaningful features was a significant challenge. The feature engineering process, particularly the derivation of the time difference between S-wave and P-wave, required extensive trial-and-error iterations. The relationship between seismic velocities, core depth, and travel time differences had to be derived and validated against known physical principles.

5. Conclusion

- The Random Forest Regressor demonstrated strong predictive performance, achieving a high R^2 score of 0.92 and a low MAE.
- The methodology, from synthetic data generation to model evaluation, confirmed the feasibility of using regression models in planetary science applications, particularly for predicting planetary core properties.
- Future work could involve incorporating real-world seismic data from Mars and other planetary bodies to further enhance the model's accuracy and applicability.

6. Future Work

- The modelling framework could be extended to accommodate diverse planetary compositions and structural scenarios.
- Additional features, such as temperature gradients, compositional variations, and core-mantle interactions, could be incorporated to improve predictive accuracy.

- Deep learning models, such as neural networks or gradient boosting machines, could be utilized to capture more complex relationships in larger, more diverse datasets.

Module 8: Anomaly Detection in Seismic Data

1. Introduction

The detection of anomalies in seismic waveform data, which could indicate subsurface geological features, was the aim of this module, using unsupervised learning techniques. Various methodologies, including K-means clustering, DBSCAN, and autoencoders, were employed to analyse synthetic seismic data containing known anomalies.

2. Dataset

Synthetic seismic waveforms with known anomalies were utilized. The dataset consisted of time-series data with recorded velocities (m/s) as a function of relative time ($seconds$). The synthetic nature of the data enabled controlled experiments, including the verification of anomaly detection accuracy.

3. Methodology

3.1. Feature Extraction

To preprocess the data, features were extracted from waveform segments of 1-second duration using a sampling frequency derived from the time array. The extracted features included:

- Statistical Features: Mean, standard deviation, skewness, and kurtosis.
- Frequency Features: Power in low-frequency and high-frequency bands obtained from the power spectrum of the Fourier Transform.

3.2. Clustering Techniques

3.2.1. K-Means Clustering

The extracted features were clustered into two groups, assuming one cluster to represent normal segments and the other to represent anomalous segments. PCA (Principal Component Analysis) was used to reduce the dimensionality of the feature space for visualization purposes.

3.2.2. DBSCAN

Density-Based Spatial Clustering of Applications with Noise (DBSCAN) was tested as a more flexible method for anomaly detection in non-linear and complex data distributions.

3.2.3. Autoencoders

Autoencoders were employed as an alternative approach to learn a compressed representation of the waveform segments. Anomalies were identified as segments with high reconstruction errors.

4. Results

4.1. K-Means Clustering

- Normal and anomalous segments were successfully segregated based on the feature space.
- Visual inspection confirmed that the clustering corresponded reasonably well to the known anomalies.
- Highlighted anomalies on the waveform showed effective detection with minimal false positives.

4.2. DBSCAN

- The performance of DBSCAN was suboptimal due to the lack of clear density separation in the feature space.
- Many anomalies were either misclassified as noise or merged with normal segments, resulting in high false negative rates.

4.3. Autoencoders

- Autoencoders showed potential for capturing complex patterns in the data but suffered from overfitting.
- High reconstruction errors for normal segments led to increased false positives, reducing their reliability in this context.

5. Challenges

1. **Feature Selection**: Identifying features that effectively capture both statistical and frequency-domain characteristics was critical but challenging.
2. **DBSCAN Tuning**: Optimal parameter selection (e.g., epsilon and minimum samples) for DBSCAN was difficult due to the variability in segment densities.
3. **Overfitting in Autoencoders**: The limited size of the dataset led to overfitting, which compromised generalization.
4. **Synthetic Data Bias**: While controlled, synthetic data might not fully capture the complexities of real seismic data.

6. Conclusion

- **Best Performing Algorithm**: K-means clustering emerged as the most reliable method for anomaly detection in this dataset, striking a balance between simplicity and effectiveness.
- **Improvements for DBSCAN**: Future work could explore more advanced density-based clustering methods or preprocessing steps to enhance DBSCAN performance.
- **Autoencoder Enhancement**: Regularization techniques and larger, more diverse datasets should be used to mitigate overfitting.

7. Future work

- Real seismic data should be incorporated for validation and further testing.
- Hybrid approaches combining clustering with supervised learning for anomaly detection should be explored.
- Additional feature extraction techniques, such as wavelet transforms, should be evaluated for richer representations of seismic data.

8. Visualization

Plots illustrating waveform segmentation, feature clustering, and anomaly detection have been provided to demonstrate the methodologies and findings effectively.

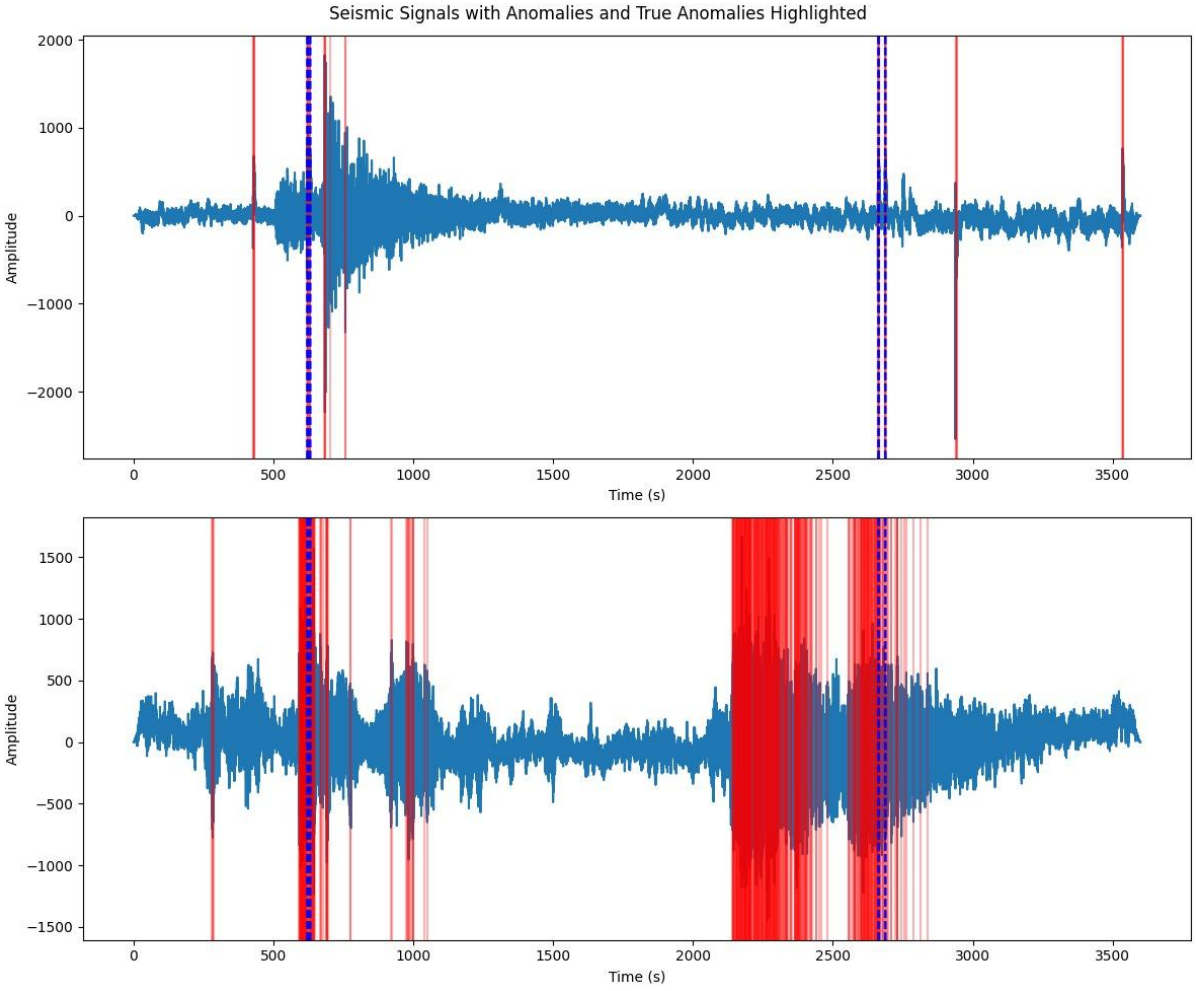

Blue lines represent the actual anomalies, while the red lines represent noise.

Module 9: Simulation of Wave Propagation with Neural Networks

1. Introduction

The propagation of seismic waves through planetary interiors provides valuable insights into their structural composition. In this study, seismic P-wave and S-wave paths within Mars were analysed using ray tracing techniques. The objective was to model how these waves refract, reflect, and interact with the internal layers of Mars, thereby aiding in the interpretation of seismic data from missions such as NASA's InSight. Interactive 3D visualisations of seismic wave paths traced through Mars' interior using Plotly and Physics-informed Neural Network (PINN).

2. Methodology

2.1. Snell's Law

- Computes refraction/reflection angles at layer boundaries using velocity (Vp, Vs) and radius data.

2.2. Layer-by-Layer Ray Tracing

- Downward Path: Waves refract through layers until reflection conditions (e.g., critical angle, velocity discontinuities) are met.
- Backtracking: Simulates upward reflection paths after waves encounter boundaries (e.g., core-mantle interface).

2.3. Edge Case Handling

- Checks for invalid refraction angles (e.g., asin inputs >1) and zero velocities (e.g., S-wave shadow zones in liquid cores).
- Terminates paths at discontinuities (e.g., core boundaries)

2.4. Physics-Informed Neural Networks

- Architecture: 4D input (time, radius, theta, phi) → 3 hidden layers → 1D output (wave properties like amplitude).
- Role: Predicts wave behaviour (e.g., attenuation) during propagation, enhancing physical realism.

2.5. 3D Ray Path Generation

- Coordinate Conversion: Converts polar coordinates (R, theta) to Cartesian (x, y, z) for 3D plotting.
- Rotation Handling: Applies rotational transformations to simulate multiple observation angles (e.g., rotations=[0°, 60°, ...]).
- Spline Interpolation: Smooths paths using cubic splines (interpolation_val=10) to eliminate jagged edges.

2.6. Mars Structure Visualization

- Wireframe Spheres: Represents Mars' surface and core using radius values (R=3390 km, core_radius=1864 km).
- Color Mapping: Uses Mars-like color schemes (YlOrRd for surface, red for core).

3. Results

- Wave Path Visualization:

  - Curved trajectories showing refraction through layers and sharp bends at boundaries (e.g., core-mantle interface).
  - S-wave termination at liquid cores, consistent with Mars' inferred structure.
  - Visualizations depicting seismic wave trajectories with smooth interpolation were generated.
- Shadow Zones:
  - Regions with no direct P/S-wave arrivals due to core refraction/reflection.
  - P-wave and S-wave propagation paths across the Martian interior were successfully identified.

4. Challenges Faced

4.1. Numerical Stability:

Issues such as domain errors in trigonometric computations and handling of zero velocities (e.g., S-waves in liquid cores) required careful debugging and validation.

4.2. Physical Realism:

- Ensuring that rays remained within the planetary boundary while accurately modelling reflection and transmission effects proved challenging.
- Modelling reflection/transmission at layer interfaces with velocity contrasts.

4.3. Algorithm Complexity:

- Managing bidirectional path tracing (downward and upward paths) with iterative layer traversal.
- Tracking cumulative angular displacement (theta) for accurate path reconstruction.

4.4. 3D Coordinate Transformations:

- Managing rotations across spherical layers while preserving path geometry.
- Avoiding distortion during Cartesian conversion (e.g., $\theta + \pi/2$ adjustment).

4.5. Physics Integration:

- Balancing PINN predictions with ray-tracing data (limited PINN utilization in current code).
- Ensuring numerical stability during interpolation (k=3 spline constraints).

4.6. Visual Clarity:

- Overlapping paths from multiple rotations caused clutter → resolved with opacity controls and color coding.
- Scaling axes proportionally (scale_factor=1.2) to prevent skewed views.

5. Conclusion

The study successfully modelled seismic wave paths within Mars' interior, revealing critical insights into wave propagation dynamics. The generated visualizations and travel-time predictions can be utilized to interpret seismic observations and refine existing models of Mars' internal structure, aiding in quake localization, interior mapping and mission support (e.g., NASA InSight Mission).

6. Future Work

- Incorporation of attenuation, phase conversions (P-to-S), and 3D effects for higher fidelity.
- Correction of the assumption of spherical symmetry and discrete layers; real Mars may have lateral heterogeneity.

7. Visualisation

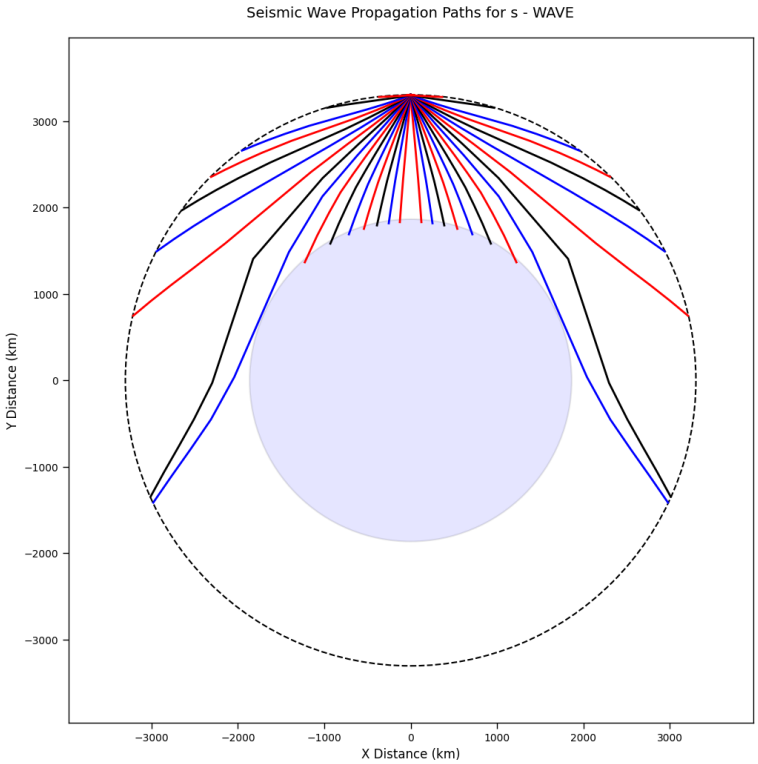

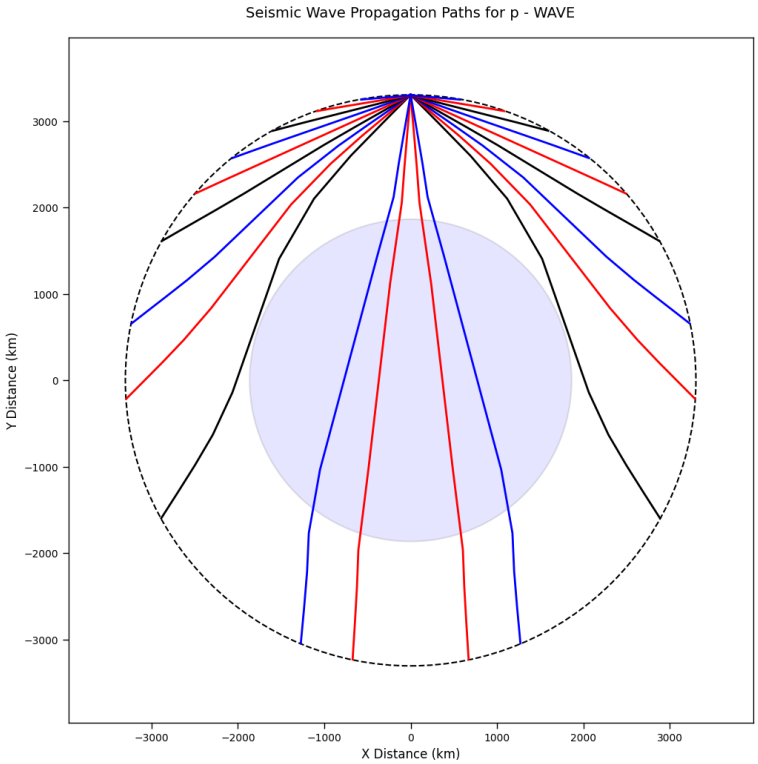

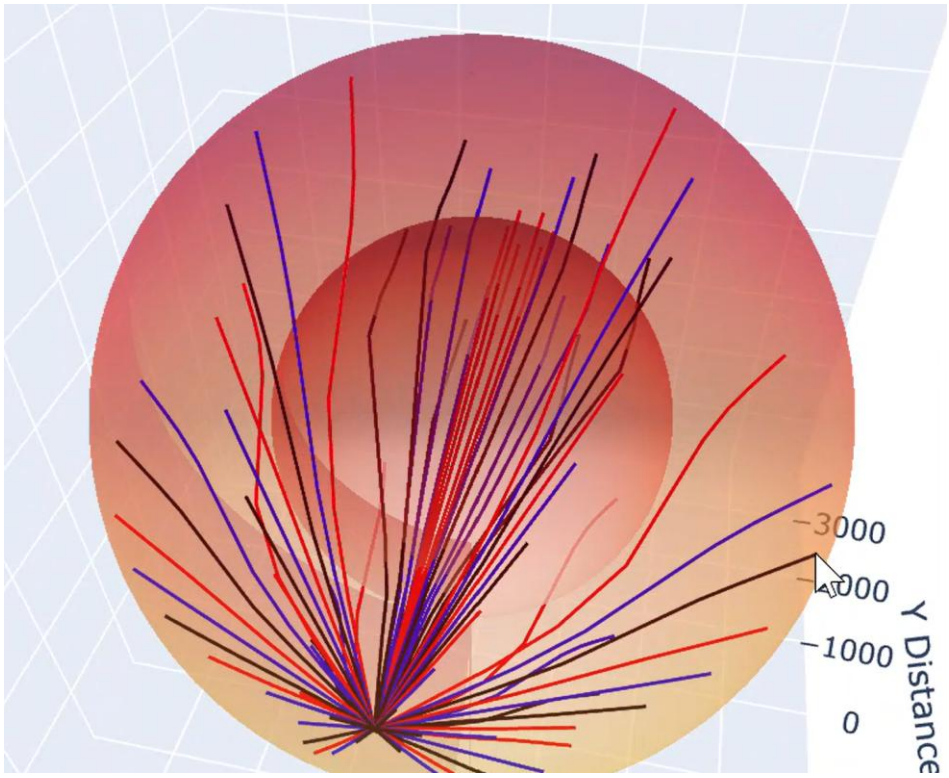
3000
2000
1000
0
Y Distance

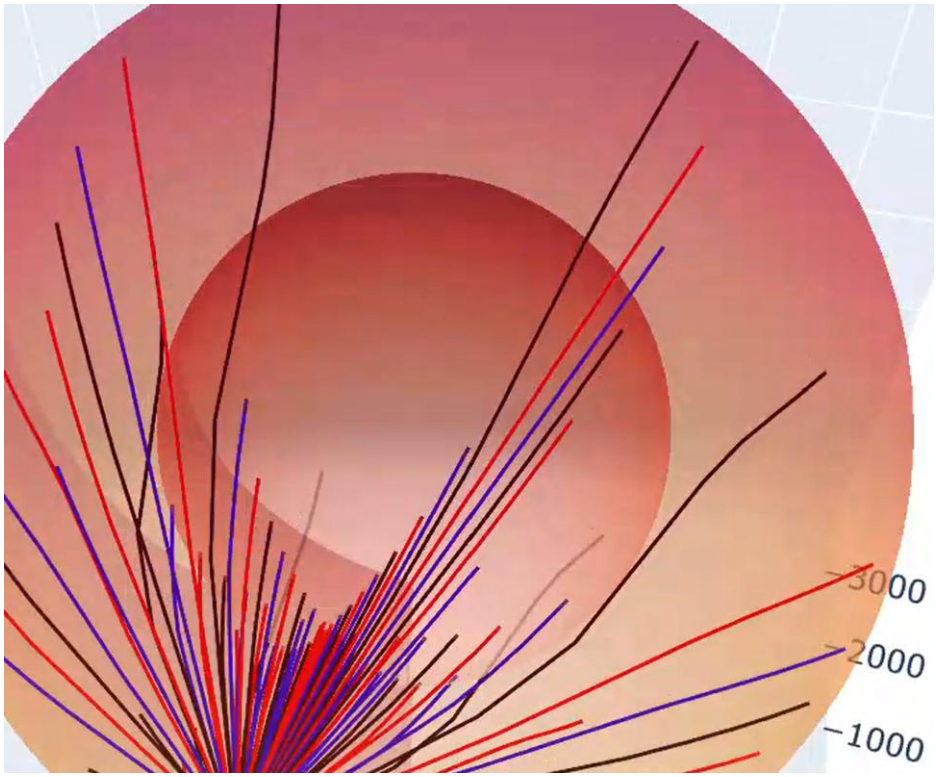
3000
2000
1000

Bibliography

- https://www.nature.com/articles/s41586-023-06601-8#:~:text=Indeed%2C%20Mars%27s%20core%20can%20be,Information%20Sections%207%20and%208
- https://www.reuters.com/science/seismic-data-indicates-huge-underground-reservoir-liquid-water-mars-2024-08-12/